# Communication-Free Grid-Supportive Control of Converter-Based ZIP Loads in DC Microgrids

Ömer Ekin, *Graduate Student Member, IEEE*, Moein Ghadrdan, *Member, IEEE*, Giovanni De Carne, *Senior Member, IEEE*, Veit Hagenmeyer, *Member, IEEE*

***Abstract*—In recent years, DC microgrids have garnered significant attention due to their superior capability in integrating renewable energy sources. However, the predominance of renewables in these systems introduces increased uncertainty in power generation, thereby elevating the risk of load loss. While the integration of energy storage systems is widely regarded as the primary solution to mitigate this issue, load-side grid support has also been proposed as a viable alternative strategy. This paper proposes a communication-free grid-supportive load (GSL) controller for converter-based constant-impedance/current/power (ZIP) loads, enabling local voltage support using only bus-voltage measurements. First, a unified control strategy is introduced that dynamically adjusts the load-side voltage reference via a saturation-plus-hysteresis mechanism, ensuring device safety while enabling grid support. Second, an energy-based restoration scheme is proposed that tracks cumulative power deviations and smoothly returns the load to nominal operation, avoiding rebound transients. Finally, the concept is experimentally validated on a $700\,\mathrm{V}$, $14\,\mathrm{kW}$ DC microgrid. Under a 4 kW load step, the proposed scheme reduces the voltage dip by $12.9\,\%$ and prevents converter shutdown when the battery reaches its power limit, outperforming a conventional PI-controlled system. The results demonstrate that local, device-embedded control of ZIP loads can deliver effective grid support without requiring communication or additional energy storage.**

***Index Terms*—DC microgrid, Distributed control, Grid-supportive loads, ZIP loads**

## NOMENCLATURE

| | |
|---|---|
| $V_{\mathrm{DC}}$ | Measured DC-bus voltage, [V] |
| $V^*_{\mathrm{DC}}$ | Reference DC-bus voltage, [V] |
| $C_{\mathrm{DC}}$ | DC-bus capacitance, [F] |
| $R'_{\mathrm{B1}}$, $R'_{\mathrm{Ld}i}$ | Equivalent damping resistance of battery/load converter, [Ω] |
| $V_{\mathrm{Ld}i}$ | Measured terminal voltage of load $i$, [V] |
| $V^*_{\mathrm{Ld}i}$ | Reference voltage of load $i$, [V] |
| $V^{\mathrm{nom}}_{\mathrm{Ld}i}$ | Nominal voltage rating of load $i$, [V] |
| $I_{\mathrm{Ld}i}/I^*_{\mathrm{Ld}i}$ | Measured/Reference current of load $i$, [A] |
| $u_{\mathrm{Ld}i}$ | Duty cycle of the converter for load $i$, [-] |
| $k_{\mathrm{GS},i}$ | Grid-support gain for load $i$, [-] |
| $\sigma_i$ | Maximum admissible voltage deviation for load $i$, [p.u.] |
| $\rho_i$ | Dead-band parameter for load $i$, [p.u.] |
| $\Lambda_i$ | Hysteresis band parameter for load $i$, [p.u.] |
| $\xi_i$ | Intermediate voltage-deviation factor, [-] |
| $\xi_{\mathrm{Ld}i}$ | Voltage-adjustment factor for load $i$, [-] |
| $\mathcal{H}_i$ | Hysteresis state indicator for load $i$, [-] |
| $\theta$ | Restoration variable (1: full support, 0: restoration mode), [-] |
| $K_{P1,i}$, $K_{I1,i}$ | Current-loop PI gains for load $i$, [-] |
| $K_{P2,i}$, $K_{I2,i}$ | Voltage-loop PI gains for load $i$, [-] |
| $P_0$ | Nominal ZIP load power, [W] |
| $V_0$ | Nominal ZIP load voltage used for normalization, [V] |
| $P_{\mathrm{Ld}i}$ | Instantaneous power of ZIP load $i$, [W] |
| $P_P$, $P_I$, $P_Z$ | Constant-power, current, and impedance components of ZIP load $i$, [W] |
| $i'_{\mathrm{Ld}}$ | Equivalent input current of converter-based load, [A] |
| $G_{\mathrm{gsl}}$ | Incremental input conductance induced by GSL action, [S] |
| $\alpha$ | Voltage ratio $\alpha = V^{\mathrm{nom}}_{\mathrm{Ld}}/V^*_{\mathrm{DC}}$, [-] |
| $P_{\mathrm{step}}$ | Load step change, [W] |
| $P_{\mathrm{GSL}}$ | Instantaneous power of the GSL load, [W] |
| $P_{\mathrm{nom}}$ | Nominal power of the GSL load, [W] |
| $E^{\max}_{\mathrm{GSL}}$ | Maximum allowable energy deviation before restoration, [W h] |
| $\Xi^{\max}_{\mathrm{GSL}}$ | Normalized maximum permissible energy deviation of load $i$, [-] |
| $w_P$, $w_I$, $w_Z$ | ZIP model weighting coefficients (constant-power, current, impedance), [-] |
| $T_p$ | Time window for integrating power deviations, [s] |
| $T_{\mathrm{res}}$ | Duration of restoration phase, [s] |
| $T_{\mathrm{rec}}$ | Recovery duration at nominal operation before GSL is re-enabled, [s] |

This work has been supported by the Helmholtz Association under the program "Energy System Design" and under the Helmholtz Young Investigator Group "Hybrid Networks" (VH-NG-1613).

## I. INTRODUCTION

THE increasing integration of renewable energy sources into modern power systems has led to a widespread deployment of power-electronic converters [1]. These converters facilitate the efficient and flexible coupling of distributed generation units, particularly photovoltaics and wind turbines, to the grid. However, the inherently intermittent and non-dispatchable nature of such sources introduces fluctuations in power output. Consequently, maintaining generation-demand power equality and stability requires fast and accurate real-time balancing mechanisms to compensate for these generation uncertainties [2].

Battery energy storage systems (BESS) are widely employed to buffer the mismatch between generation and demand [3], [4]. They absorb surplus energy during periods

This article has been accepted for publication in IEEE Journal of Emerging and Selected Topics in Power Electronics. This is the author's version which has not been fully edited and content may change prior to final publication. Citation information: DOI 10.1109/JESTPE.2026.3651885



of overproduction and release it during generation shortfalls. However, as the share of converter-interfaced renewables continues to grow, both the magnitude and frequency of power fluctuations intensify. Addressing these dynamics by merely increasing storage capacity or installing additional BESS units is neither economically scalable nor environmentally sustainable, due to the high costs, material requirements, and lifecycle impacts associated with battery technologies. BESS units therefore remain a cornerstone of microgrid operation, but there is increasing interest in complementing them with demand-side flexibility in order to reduce the required storage rating and to improve local damping without adding further storage hardware.

An emerging complementary solution is the integration of grid-supportive loads (GSLs), which autonomously modulate their power consumption in response to local grid conditions [5]. Unlike traditional passive loads, GSLs dynamically adapt their demand to provide ancillary services such as voltage and frequency stabilization, thereby reducing stress on centralized storage and enhancing overall system flexibility. This concept represents a promising avenue for achieving scalable, low-cost, and communication-free balancing strategies in converter-dominated power systems [6].

In this context, a GSL is a converter-interfaced load whose power consumption is deliberately modulated as a function of local electrical variables, while respecting device-level operating constraints. In practice, suitable candidates are loads with an inherent energy buffer that can tolerate short-term power deviations without compromising their primary service. Typical examples include heating and cooling systems with thermal inertia. In particular, a GSL does not create additional energy in the system. Instead, it temporarily reshapes its instantaneous power consumption around a nominal profile by exploiting the inherent energy buffer of the underlying process. For example, a refrigerator can reduce its power during a voltage dip by using stored thermal energy and later increase its power to restore the temperature. Over the relevant time horizon, the net energy consumption may remain unchanged, but on short time scales the controlled power deviation behaves similarly to a small distributed storage unit and contributes to voltage support. In the proposed control framework, this flexibility is represented by an energy-deviation state and the bound $E_{\mathrm{GSL}}^{\max}$, which define the admissible deviation from the nominal energy content and trigger restoration once this budget is exhausted.

Fig. 1 illustrates a simplified DC microgrid representation, highlighting the typical components of renewable generation, storage, and demand. While BESS have traditionally been the main source of flexibility, the figure emphasizes that loads themselves may also be leveraged as active participants in grid support. The concept of grid-supportive loads has been extensively investigated in AC power systems. A well-established approach is demand-side frequency response, where aggregations of thermostatically controlled appliances are coordinated to deliver fast frequency support and improve system stability during contingencies [5]. A frequency-based power control strategy was introduced in [7], wherein the frequency on the secondary side of a solid-state transformer

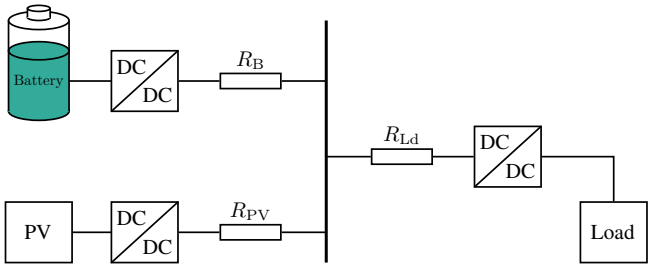


Fig. 1. Simplified representation of a DC microgrid, aggregated to its essential components: a PV generator, a battery energy storage system, and a load.

is regulated to manage power consumption within the low-voltage (LV) distribution grid. Building upon this approach, [8] further extended the study by deriving the power-to-frequency sensitivity coefficients necessary for implementing real-time control mechanisms. In [9], variable-speed drive appliances were shown to autonomously adjust their power consumption in response to local frequency deviations, thereby providing fast frequency response without communication. Similarly, [10] proposed a grid-supportive power modulation algorithm for inverter-based motor loads, demonstrating through simulations and hardware experiments that sub-second frequency regulation can be achieved reliably. Collectively, these studies confirm that AC-side GSLs can provide frequency regulation, and inertial response without requiring communication infrastructure or compromising end-user comfort.

Compared to AC systems, DC microgrids remain far less explored in the context of GSLs. The absence of a global frequency signal, combined with inherently faster voltage dynamics, poses unique challenges for decentralized control. Unlike AC grids, where kinetic energy in rotating machines provides short-term inertia, energy buffering in DC microgrids relies almost exclusively on the DC-bus capacitor. However, the capacitance is typically limited due to cost, volume, and lifetime constraints, and increasing it aggravates fault current severity due to rapid discharge behavior [11]–[13].

In DC microgrids with constant-power loads (CPLs), shaping the load dynamics is a well-established approach to improve bus-voltage stability. Virtual capacitor control, for example, modifies the power reference of a constant-power load by adding a term proportional to $V_{\mathrm{DC}}\dot{V}_{\mathrm{DC}}$, which makes the load behave as if an additional capacitor were connected in parallel to the DC bus [14]. These methods, however, primarily target constant-power loads and do not explicitly consider the more general case of mixed load compositions.

DC electric springs are also introduced in [15], [16] as an alternative solution for providing temporary voltage support in DC microgrids, where multiple DC electric springs collaboratively regulate the bus voltage. These devices not only stabilize the DC link but can also emulate virtual inertia, providing damping against fast disturbances. However, their deployment requires additional converter hardware and control complexity at each participating load, which may limit scalability and cost-effectiveness in practical DC microgrids.

Emerging low-voltage DC standards also promote the use of the bus voltage as a coordination signal, which naturally leads

to $P$–$V$ or $I$–$V$ load droop characteristics for dispatchable loads. Under ideal conditions, such load droop converts the negative incremental resistance of a constant-power load into a positive, damping conductance and can therefore eliminate the classical minimum-capacitance constraint [17]. This methodology however, is primarily tailored for individual loads, employing distinct predefined droop characteristics for each load according to its tolerance to voltage deviations. In contrast, the GSL approach can accommodate load points with dynamic behavior, responding adaptively through a load sensitivity system that continuously analyzes and updates load coefficients.

A fully decentralized GSL control strategy that relies solely on local bus voltage measurements has been proposed in [18] . By combining droop-based voltage–power characteristics with hysteresis logic, this approach enables converter-interfaced resistive loads to autonomously stabilize the DC-bus voltage without requiring additional hardware or communication infrastructure. In [19], this concept is further developed by extending the hysteresis-based GSL controller and providing practical tuning guidelines to reduce chattering and improve dynamic performance. However, the validation in [18], [19] is limited to simulations, the modeling considers only resistive loads, and no mechanism for energy-based restoration or rebound prevention is included.

In practice however, converter-interfaced loads often exhibit a mixture of constant-impedance, constant-current, and constant-power behavior. The well-established ZIP (constant impedance, constant current, constant power) load model captures these effects in a unified framework and allows systematic assessment of their impact on the bus voltage stability [20], [21]. The effectiveness of grid-supportive control strategies is closely tied to the underlying ZIP load composition. Impedance-dominated loads enhance system damping and can positively influence power balancing. Constant-current loads also offer moderate support, whereas constant-power loads, due to their fixed power consumption, inherently lack the ability to contribute to generation-load balancing. Extending grid-supportive control from purely resistive to generalized ZIP behavior is therefore essential for realistic modeling and practical applicability.

Moreover, existing GSL studies lack validation in experimentally representative setups that include converter-based loads, line impedance effects, and dynamic interactions with controlled battery systems. An essential but often overlooked aspect of GSL control is the ability of a load to autonomously return to its nominal operating point after providing temporary support. This so-called restoration mechanism ensures that the load resumes its intended function once the disturbance has been mitigated, thereby preserving long-term service quality, user comfort, or operational constraints. In many practical applications, sustained deviation from nominal behavior is not acceptable—for example, in thermal systems, electric vehicle charging, or industrial processes. However, existing GSL control strategies rarely incorporate such mechanisms, limiting their applicability in real-world settings.

To close these gaps, this paper proposes a novel grid-supportive load control strategy tailored for converter-based loads in low-voltage DC microgrids. The proposed approach generalizes beyond resistive behavior by incorporating a full ZIP load model and modulates the load reference voltage based solely on local bus voltage measurements. An energy-aware restoration function guarantees smooth return to nominal operation after transient support phases.

The main contributions of this paper are as follows:

1) A fully decentralized control scheme for grid-supportive ZIP loads in low-voltage DC microgrids, relying solely on local bus voltage measurements without requiring communication or external coordination.
2) A generalized voltage-reference modulation strategy that extends beyond resistive loads to arbitrary combinations of constant-impedance, constant-current, and constant-power behavior.
3) A novel energy-aware restoration mechanism that ensures smooth and bounded recovery of the load's nominal operation after providing transient grid support.

These contributions are complemented by a theoretical analysis of the closed-loop system, including steady-state conditions and small-signal stability in the presence of dynamic ZIP–BESS interactions. Furthermore, the proposed control concept is experimentally validated on a laboratory-scale $700\,\mathrm{V}$ DC microgrid, featuring distributed battery systems, converter-based loads, and realistic line impedance effects.

The remainder of this paper is organized as follows. Section II introduces the microgrid architecture and its underlying dynamic models. Section III presents the proposed GSL control scheme, including the voltage-based modulation and energy-aware restoration mechanism. Section IV provides a theoretical analysis of the closed-loop stability under the proposed control. Section V presents the simulation results. Section VI describes the experimental setup and validates the control concept. Finally, Section VII concludes the paper.

## II. DC Microgrid System Description

This section describes the configuration and modeling of the evaluated DC microgrid, building on the framework established in [18], [19]. Fig. 2 depicts the $700\,\mathrm{V}$ microgrid testbench employed for both modeling and hardware validation. Three power–electronic subsystems share a common DC-bus:

1) Battery energy-storage system (BESS) connected through a bidirectional DC-DC converter. In islanded operation, the BESS is operated in grid-forming mode to establish the DC-bus voltage and buffer net power imbalances. The control is implemented via a cascaded PI controller.
2) Photovoltaic (PV) array interfaced by a unidirectional boost stage. A perturb-and-observe MPPT algorithm maximizes the PV power.
3) Converter-based ZIP load modelled as a programmable combination of constant-impedance (Z), constant-current (I) and constant-power (P) demand, and supplied through a bidirectional DC-DC converter. The proposed grid-supportive control strategy is implemented on this converter.

In this work, the BESS operates in grid-forming mode and establishes the DC-bus voltage reference $V_{\mathrm{DC}}^{*}$, while buffering

This article has been accepted for publication in IEEE Journal of Emerging and Selected Topics in Power Electronics. This is the author's version which has not been fully edited and content may change prior to final publication. Citation information: DOI 10.1109/JESTPE.2026.3651885



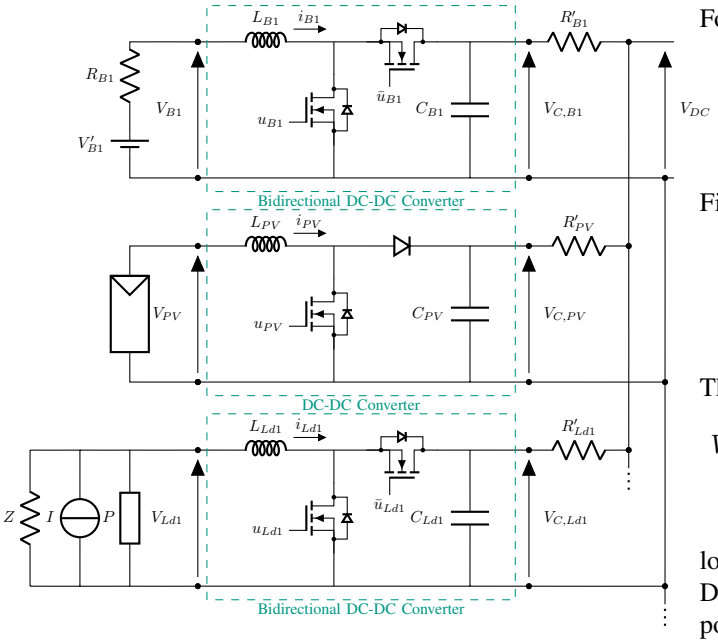


Fig. 2. Electrical circuit of the DC microgrid comprising an energy storage, a photovoltaic unit as an RES, and ZIP loads.

net power imbalances in the microgrid. This choice reflects a typical architecture for islanded DC systems, but it is not a fundamental requirement of the proposed GSL concept. In principle, the same load-side controller can also be combined with other grid-forming units, such as an upstream AC/DC converter. In the absence of grid forming units, however, GSL action alone cannot compensate a sustained power deficit or surplus; it can only reshape the demand profile over short time intervals and thereby mitigate the resulting voltage excursions. An averaged state–space model is employed to capture the dominant bus–converter dynamics and to serve as the basis for the subsequent stability analysis and control design.

### A. Averaged state–space model

As previously discussed, in this study the BESS functions as the grid-forming unit, maintaining the voltage within a limited range around its reference value. The proposed GSL control strategy operates as a complementary mechanism, further reducing the voltage variation range to enhance regulation performance. Therefore, it is reasonable to perform the average state-space analysis in the vicinity of the reference operating point. Operating points with deeply depressed DC-bus voltages, where devices approach their minimum operating limits or change conduction mode, are outside the scope of the present analysis.

The BESS dynamics are

$$\dot{i}_{\mathrm{B1}} = \frac{V_{\mathrm{B1}}}{L_{\mathrm{B1}}} - \frac{R_{\mathrm{B1}}}{L_{\mathrm{B1}}} i_{\mathrm{B1}} - \frac{V_{C,\mathrm{B1}}}{L_{\mathrm{B1}}} u_{\mathrm{B1}}, \tag{1}$$

$$\dot{V}_{C,\mathrm{B1}} = \frac{V_{\mathrm{DC}} - V_{C,\mathrm{B1}}}{C_{\mathrm{B1}} R'_{\mathrm{B1}}} + \frac{i_{\mathrm{B1}}}{C_{\mathrm{B1}}} u_{\mathrm{B1}}. \tag{2}$$

For the PV boost stage

$$\dot{i}_{\mathrm{PV}} = \frac{V_{\mathrm{PV}}}{L_{\mathrm{PV}}} - \frac{R_{\mathrm{PV}} + R_D}{L_{\mathrm{PV}}} i_{\mathrm{PV}} - \frac{V_{C,\mathrm{PV}}}{L_{\mathrm{PV}}} u_{\mathrm{PV}}, \tag{3}$$

$$\dot{V}_{C,\mathrm{PV}} = \frac{V_{\mathrm{DC}} - V_{C,\mathrm{PV}}}{C_{\mathrm{PV}} R'_{\mathrm{PV}}} + \frac{i_{\mathrm{PV}}}{C_{\mathrm{PV}}} u_{\mathrm{PV}}. \tag{4}$$

Finally, the $i$-th load DC-DC converter is described by

$$\dot{i}_{\mathrm{Ld}i} = \frac{V_{C,\mathrm{Ld}i}}{L_{\mathrm{Ld}i}} u_{\mathrm{Ld}i} - \frac{V_{\mathrm{Ld}i}}{L_{\mathrm{Ld}i}} - \frac{R_{\mathrm{Ld}i}}{L_{\mathrm{Ld}i}} i_{\mathrm{Ld}i}, \tag{5}$$

$$\dot{V}_{C,\mathrm{Ld}i} = \frac{V_{\mathrm{DC}} - V_{C,\mathrm{Ld}i}}{C_{\mathrm{Ld}i} R'_{\mathrm{Ld}i}} - \frac{i_{\mathrm{Ld}i}}{C_{\mathrm{Ld}i}} u_{\mathrm{Ld}i}. \tag{6}$$

The common DC-bus capacitor $C_{\mathrm{DC}}$ closes the system via

$$\dot{V}_{\mathrm{DC}} = \frac{V_{C,\mathrm{B1}} - V_{\mathrm{DC}}}{C_{\mathrm{DC}} R'_{\mathrm{B1}}} + \frac{V_{C,\mathrm{PV}} - V_{\mathrm{DC}}}{C_{\mathrm{DC}} R'_{\mathrm{PV}}} + \sum_i \frac{V_{C,\mathrm{Ld}i} - V_{\mathrm{DC}}}{C_{\mathrm{DC}} R'_{\mathrm{Ld}i}}. \tag{7}$$

To enable voltage-based control of converter-interfaced loads and to analyze their dynamic interaction with the DC-bus, it is essential to mathematically characterize their power–voltage relationship. In this work, loads are represented by a generalized ZIP model that combines constant-impedance, constant-current, and constant-power behavior, capturing the diverse characteristics of modern electronic devices.

### B. ZIP load characterisation

The instantaneous power drawn by a ZIP load is expressed as

$$P_{\mathrm{Ld}i} = P_0 \cdot \Big( \underbrace{w_{\mathrm{P}}}_{\substack{\text{const.}\\ \text{Power}}} + \underbrace{w_{\mathrm{I}} \frac{V_{\mathrm{Ld}i}}{V_0}}_{\substack{\text{const.}\\ \text{Current}}} + \underbrace{w_{\mathrm{Z}} \left( \frac{V_{\mathrm{Ld}i}}{V_0} \right)^2}_{\substack{\text{const.}\\ \text{Impedance}}} \Big), \tag{8}$$

where $P_0$ and $V_0$ denote the nominal operating point. Throughout this work, the ZIP coefficients are assumed to be non-negative and to satisfy $w_{\mathrm{P}} + w_{\mathrm{I}} + w_{\mathrm{Z}} = 1$, such that $P_0$ represents the total nominal load power. The extreme cases of the ZIP model are also included in this framework: a purely constant-power load corresponds to $w_{\mathrm{P}} = 1$ and $w_{\mathrm{I}} = w_{\mathrm{Z}} = 0$, while a purely constant-current load is obtained for $w_{\mathrm{I}} = 1$ and $w_{\mathrm{P}} = w_{\mathrm{Z}} = 0$. The individual contributions of the ZIP components at a given operating point can also be expressed in terms of their absolute power contributions:

$$P_P := P_0 w_P, \quad P_I := P_0 w_I, \quad P_Z := P_0 w_Z. \tag{9}$$

Here, $P_P$, $P_I$, and $P_Z$ represent the constant power, current-proportional, and impedance-proportional parts of the total load power, respectively. Equation (8) enables the quadratic voltage–power mapping used later in Section III to generalize the grid-supportive action from purely resistive to arbitrary ZIP loads.

## III. Grid-supportive Load Control

This section presents the proposed GSL control method, designed to enhance interfaced ZIP loads with grid-support capabilities. The control method relies solely on the locally measured DC-bus voltage and combines (i) voltage-reference modulation for fast disturbance mitigation with (ii) energy-based

restoration that returns the device smoothly to its nominal operating point. The overall structure is depicted in Fig. 3; notation is presented in the Nomenclature.

### A. Voltage-reference Adjustment

The GSL control adjusts the reference voltage of the $i^{\text{th}}$ load to modulate its power, mitigating DC-bus voltage deviations in the microgrid. The reference voltage of the $i^{\text{th}}$ load is defined as:

$$V^{*}_{\text{Ld}i} = V^{\text{nom}}_{\text{Ld}i} \cdot \xi_{\text{Ld}i} \tag{10}$$

where the scaling factor $\xi_{\text{Ld}i}$ is determined by:

$$\xi_{\text{Ldi}} = \begin{cases} 1+\sigma_i, & \text{if } \xi_i \geq 1+\sigma_i \\ 1-\sigma_i, & \text{if } \xi_i \leq 1-\sigma_i \\ \xi_i, & \text{otherwise} \end{cases} \tag{11}$$

with

$$\xi_i = 1 + k_{\text{GS},i} \cdot \theta \cdot \left(\frac{V_{\text{DC}}}{V^{*}_{\text{DC}}} - 1\right) \tag{12}$$

where $\sigma_i$ defines the allowable percentage deviation in voltage for the $i^{\text{th}}$ load (e.g. $\sigma_i = 0.05$ for a $5\%$ variation), $k_{\text{GS},i} > 0$ is the grid-support gain for load $i$, and $\theta \in (0,1)$ is a restoration variable, regulating the gradual return of critical loads to their nominal state. To mitigate excessive or unnecessary control actions, the hysteresis-based logic is integrated into the computation of $\xi_{\text{Ldi}}$. This mechanism ensures that the system responds only to substantial deviations, while suppressing frequent switching within a predefined tolerance band. Accordingly, the response in Equation (11) has been updated as:

$$\xi_{\text{Ldi}}(t) = \begin{cases} 1, & \text{if } \mathcal{H}_i(t) = 1 \\ \text{sat}_{[1-\sigma_i,\, 1+\sigma_i]}\big(\xi_i(t)\big), & \text{if } \mathcal{H}_i(t) = 0 \end{cases} \tag{13}$$

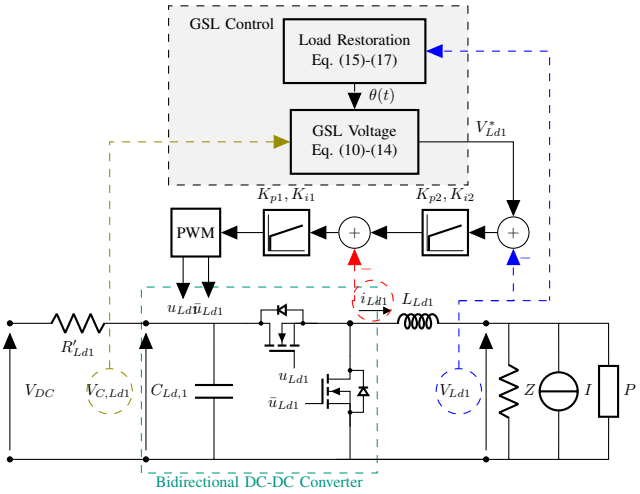


Fig. 3. Proposed GSL controller for the $i^{\text{th}}$ ZIP load. The scheme relies exclusively on local measurements, while the restoration weight $\theta$ is provided by the energy-based restoration block described in Sec. III-B.

The hysteresis state $\mathcal{H}_i(t)$ is updated according to the following rule:

$$\mathcal{H}_i(t^{+}) = \begin{cases} 0, & \mathcal{H}_i(t^{-}) = 1 \text{ and } \xi_i(t) \notin [1-\Lambda_i,\, 1+\Lambda_i] \\ 1, & \mathcal{H}_i(t^{-}) = 0 \text{ and } \xi_i(t) = 1 \\ \mathcal{H}_i(t^{-}), & \text{otherwise} \end{cases} \tag{14}$$

Here, the superscripts $t^{-}$ and $t^{+}$ denote the values immediately before and after the update at time $t$, respectively. The parameter $\Lambda_i$ specifies the hysteresis band used to suppress switching due to minor fluctuations.

### B. Load Restoration Control

Restoring critical loads after grid-supportive actions is essential to ensure the continuous operation of vital loads. The proposed restoration strategy is energy-based, allowing for a smooth transition back to nominal operation while avoiding abrupt changes that could destabilize the grid.

*1) Restoration Condition:* The restoration process begins when the cumulative energy deviation exceeds a predefined threshold $E^{\max}_{\text{GSL}}$, as expressed by:

$$\underbrace{\left(\int_{t-T_p}^{t} (P_{\text{GSL}}(\tau) - P_{\text{nom}})d\tau\right)}_{A_1} + \underbrace{\frac{T_{\text{res}}}{2}(P_{\text{GSL}}(t) - P_{\text{nom}})}_{A_2} > E^{\max}_{\text{GSL}} \tag{15}$$

where $T_p$ represents the time window for integrating power deviations, and $T_{\text{res}}$ the duration for gradual restoration to nominal power. $P_{\text{GSL}}(t)$ is the power of the GSL load at the time $t$ and $P_{\text{nom}}$ is the nominal power. $E^{\max}_{\text{GSL}}$ is the maximum allowable energy deviation before initiating restoration. This condition ensures that restoration is triggered only when necessary, preventing premature actions and unnecessary stress on the system. The area $A_1$ corresponds to the measured energy deviation from past performance, while the area $A_2$ represents the estimated energy required to return to the nominal value. Assuming significantly faster voltage and current control (time-scale separation), $\xi_{\text{Ld}i}$ can be used as a measurement variable for calculating relative energy deviations. This approach is advantageous because, for busses that accommodate multiple loads, the nominal power is not inherently known.

$$\left(\int_{t-T_p}^{t} \Big(w_{\text{I}}\big(\xi_{\text{Ld}i}(\tau) - 1\big) + w_{\text{Z}}\big(\xi_{\text{Ld}i}(\tau)^2 - 1\big)\Big)d\tau \right.$$
$$\left. + \frac{T_{\text{res}}}{2}\Big(w_{\text{I}}\big(\xi_{\text{Ld}i}(t) - 1\big) + w_{\text{Z}}\big(\xi_{\text{Ld}i}(t)^2 - 1\big)\Big)\right) > \Xi^{\max}_{\text{GSL}} \tag{16}$$

with $\Xi^{\max}_{GSi}$ being a normalized maximum permissible energy deviation of $i^{\text{th}}$ load, which depends on the characteristics of the load. This inequality determines the load's restoration start moment.

*2) Restoration Process:* Once the restoration criterion in (15) is met, the restoration process begins by gradually decreasing the restoration variable $\theta$ from 1 to 0 over the restoration time $T_{\text{res}}$. The time constants associated with the restoration loop, denoted as $T_p$ and $T_{\text{res}}$, are chosen to be several orders of magnitude longer than the electrical dynamics of the DC bus. Consequently, the restoration mechanism primarily influences the long-term energy balance of the load, while avoiding rapid voltage transients. This smooth transition prevents sudden changes in power, which could disrupt system stability. After the recovery period $T_{\text{rec}}$, the load operates at its nominal power for a defined interval before $\theta$ is gradually ramped back to 1, fully restoring the load's grid-supportive functionalities. The evolution of $\theta$ during the restoration phase is depicted in Fig. 4 as:

① **Restoration Initiation:**

$$\theta(t) = 1 - \frac{t - t_{\text{start}}}{T_{\text{res}}}, \quad t \in [t_{\text{start}}, t_{\text{start}} + T_{\text{res}}], \tag{17}$$

where $t_{\text{start}}$ is the time at which restoration begins.

② **Restoration Completion:** After the restoration phase, the load remains at its nominal state for a fixed recovery time $T_{\text{rec}}$ with $\theta(t) = 0$.

③ **Re-enabling GSL Functionality:** Finally, $\theta$ is ramped back to 1 (typically over another interval of length $T_{\text{res}}$) so that the load can resume grid-supportive actions without additional transients.

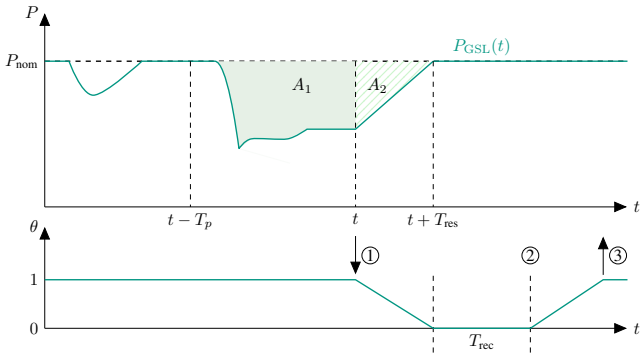


Fig. 4. Conceptual representation of the restoration method for critical loads in a DC microgrid over time. The curve illustrates the gradual restoration and prioritization of critical loads following a disruption.

## C. GSL Controller Setup and Operation

The implementation main steps for the proposed GSL controller in a generic low-voltage DC microgrid are illustrated in Fig. 5. The procedure begins by selecting converter-interfaced loads capable of providing an inherent energy buffer. Two categories of input data are also required: (i) ZIP load coefficients $(w_P, w_I, w_Z)$, obtained through load sensitivity analysis, and (ii) the local DC-link voltage, which serves as the primary indicator of generation–demand imbalance. Additionally, load specifications such as the nominal operating point $(P_0, V_0)$ and the maximum energy buffer must be defined. The voltage support gain $\sigma_i$ and hysteresis band $\Lambda_i$ are configured to ensure that the local voltage reference adaptation remains within the permissible range of standards. During operation, the GSL updates its voltage reference according to (10)-(14) using the measured DC-link voltage and evaluates the consumed support energy $E_{\text{GSL}}$ based on (15). As long as $E_{\text{GSL}} < E_{\text{GSL}}^{\max}$, the grid-supportive mode is maintained and the update cycle is repeated. Once the energy budget is exhausted, a recovery sequence is triggered, where $\theta$ is gradually decreased according to (17) and thereby the load is gradually returning to its nominal voltage reference. This nominal state is maintained for $T_{\text{rec}}$, after which the GSL functionality is gradually re-enabled.

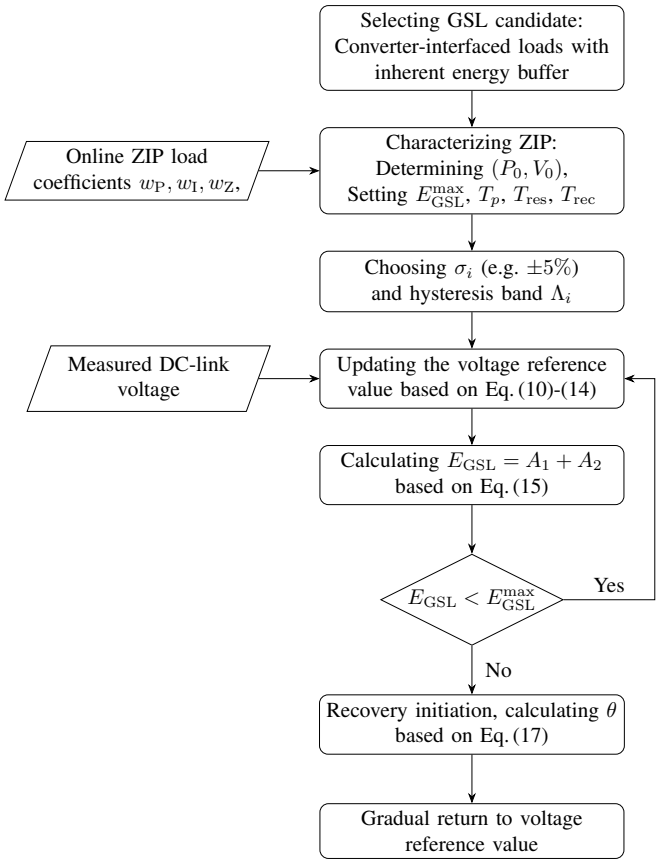


Fig. 5. Design flow for configuring grid-supportive load (GSL) control in a generic low-voltage DC microgrid.

## IV. Stability Analysis

This section proves that the proposed GSL control strategy increases the small-signal damping of the DC-bus voltage. The well-posedness of the linearization procedure is ensured under the following assumptions.

**Assumptions.** (i) Inner current/voltage loops of all converters are much faster than the DC-bus dynamics (time-scale separation), hence the load terminal voltage tracks its reference: $V_{\text{Ld}i} \approx V_{\text{Ld}i}^*$. (ii) The operating point lies strictly *inside* the saturation/hysteresis bands, such that these nonlinearities are inactive and their logic is frozen during linearization. (iii) The restoration state is fixed at $\theta = 1$ (worst-case, maximum GSL action). To analyze the effect of the GSL controller on system stability, the DC microgrid is reduced to an equivalent small-signal model. The full averaged converter models are mapped

This article has been accepted for publication in IEEE Journal of Emerging and Selected Topics in Power Electronics. This is the author's version which has not been fully edited and content may change prior to final publication. Citation information: DOI 10.1109/JESTPE.2026.3651885



to their Thevenin or Norton equivalents at the common DC-bus node, as shown in Fig. 6.

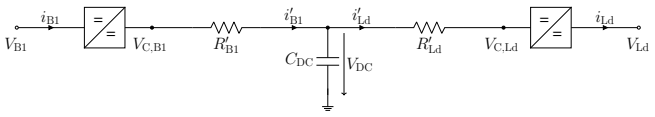


Fig. 6. Reduced equivalent circuit of the considered DC microgrid, comprising a battery storage units and a ZIP Load interfaced through DC-DC Converter.

The load converter input current equals the output power divided by the input voltage,

$$i'_{\mathrm{Ld}} \;=\; \frac{P_{\mathrm{out}}(V^*_{\mathrm{Ld}})}{V_{C,\mathrm{Ld}}}\,. \tag{18}$$

At $V_{\mathrm{Ld}} = V_0$ the ZIP equation yields

$$\left.\frac{\partial P_{\mathrm{out}}}{\partial V_{\mathrm{Ld}}}\right|_{V_0} \;=\; \frac{P_I + 2P_Z}{V_0}, \qquad P_I := P_0 w_I,\; P_Z := P_0 w_Z. \tag{19}$$

The GSL mapping is

$$\begin{aligned} V^*_{\mathrm{Ld}} &= V^{\mathrm{nom}}_{\mathrm{Ld}}\Big[1 + k_{\mathrm{GSL}}\theta\Big(\tfrac{V_{\mathrm{DC}}}{V^*_{\mathrm{DC}}} - 1\Big)\Big] \\ &\Rightarrow\; \Delta V^*_{\mathrm{Ld}} \;=\; \alpha\, k_{\mathrm{GSL}}\, \Delta V_{\mathrm{DC}}. \end{aligned} \tag{20}$$

with $\alpha := V^{\mathrm{nom}}_{\mathrm{Ld}}/V^*_{\mathrm{DC}}$ and $\theta = 1$. Linearizing $i'_{\mathrm{Ld}} = P_{\mathrm{out}}/V_{C,\mathrm{Ld}}$ at $(V^*_{C,\mathrm{Ld}}, V^*_{\mathrm{Ld}} = V_0)$ gives

$$\Delta i'_{\mathrm{Ld}} = -\frac{i'_{\mathrm{Ld},0}}{V^*_{C,\mathrm{Ld}}}\,\Delta V_{C,\mathrm{Ld}} \;+\; G_{\mathrm{gsl}}\,\Delta V_{\mathrm{DC}},$$

$$\text{with}\quad G_{\mathrm{gsl}} := \frac{\alpha\, k_{\mathrm{GSL}}}{V^*_{C,\mathrm{Ld}}}\,\frac{P_I + 2P_Z}{V_0}. \tag{21}$$

Based on the equivalent circuit representation, the dynamic behavior of the DC-bus and the load-side input capacitor can now be derived using Kirchhoff's current law (KCL). These equations form the basis of the linear time-invariant (LTI) system used for eigenvalue analysis. KCL at the bus and the input capacitor yield

$$C_{\mathrm{DC}}\Delta\dot V_{\mathrm{DC}} = -\Big(\tfrac{1}{R'_{\mathrm{B1}}} + \tfrac{1}{R'_{\mathrm{Ld}}}\Big)\Delta V_{\mathrm{DC}} + \tfrac{1}{R'_{\mathrm{Ld}}}\Delta V_{C,\mathrm{Ld}}, \tag{22}$$

$$C_{\mathrm{Ld}}\Delta\dot V_{C,\mathrm{Ld}} = \tfrac{1}{R'_{\mathrm{Ld}}}\big(\Delta V_{\mathrm{DC}} - \Delta V_{C,\mathrm{Ld}}\big) \;-\; \Delta i'_{\mathrm{Ld}}. \tag{23}$$

Substituting (21) into (23) leads to the LTI model

$$\begin{bmatrix}\Delta\dot V_{\mathrm{DC}}\\ \Delta\dot V_{C,\mathrm{Ld}}\end{bmatrix} = A\begin{bmatrix}\Delta V_{\mathrm{DC}}\\ \Delta V_{C,\mathrm{Ld}}\end{bmatrix},\quad A = \begin{bmatrix}a_{11} & a_{12}\\ a_{21} & a_{22}\end{bmatrix}, \tag{24}$$

with

$$\begin{aligned} a_{11} &= -\frac{1}{C_{\mathrm{DC}}}\Big(\frac{1}{R'_{\mathrm{B1}}} + \frac{1}{R'_{\mathrm{Ld}}}\Big), \quad a_{12} = \frac{1}{C_{\mathrm{DC}}R'_{\mathrm{Ld}}},\\ a_{21} &= \frac{1}{C_{\mathrm{Ld}}}\Big(\frac{1}{R'_{\mathrm{Ld}}} - G_{\mathrm{gsl}}\Big), \qquad a_{22} = \frac{1}{C_{\mathrm{Ld}}}\Big(-\frac{1}{R'_{\mathrm{Ld}}} + \frac{i'_{\mathrm{Ld},0}}{V^*_{C,\mathrm{Ld}}}\Big). \end{aligned} \tag{25}$$

With the system matrix defined, the influence of the GSL control on the eigenvalues of the closed-loop system can be systematically analyzed. The focus lies on how the added conductance term $G_{\mathrm{gsl}}$ influences system stability through the determinant and trace of the matrix $A$. The characteristic polynomial is $s^2 - \mathrm{tr}(A)s + \det(A) = 0$ with

$$\mathrm{tr}(A) = a_{11} + a_{22}, \qquad \det(A) = a_{11}a_{22} - a_{12}a_{21}.$$

Note that $\mathrm{tr}(A)$ is independent of $G_{\mathrm{gsl}}$, whereas

$$\det(A) \;=\; \det(A)\big|_{G_{\mathrm{gsl}}=0} \;+\; \underbrace{\frac{a_{12}}{C_{\mathrm{Ld}}}}_{>0}\,G_{\mathrm{gsl}}. \tag{26}$$

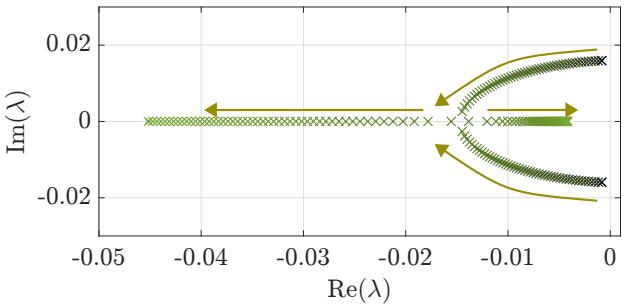


(a) Z-dominated load

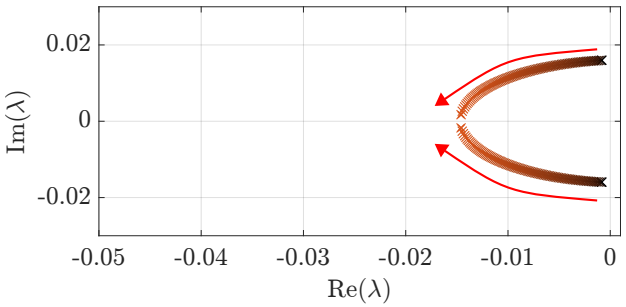


(b) I-dominated load

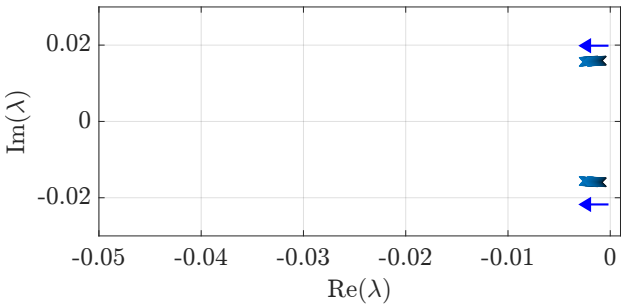


(c) P-dominated load

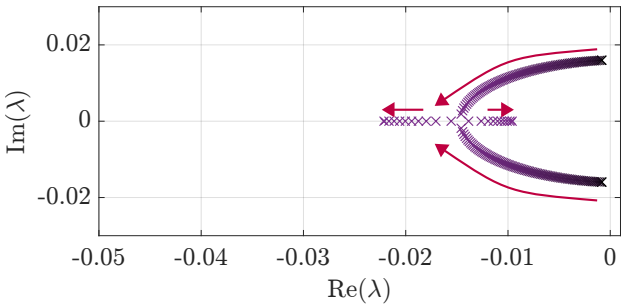


(d) Mixed ZIP load

Fig. 7. Root locus plots for varying GSL gain ($k_{\mathrm{GSL}} \in [0, 5]$) under four ZIP load scenarios. Arrows indicate eigenvalue trajectories with increasing gain.

Because $G_{\mathrm{gsl}} \propto k_{\mathrm{GSL}}\,(P_I + 2P_Z)$ by (21) and $a_{12} > 0$, the following can be obtained

$$\frac{\partial \det(A)}{\partial k_{\mathrm{GSL}}} \;>\; 0 \quad \text{for } P_I + 2P_Z \geq 0.$$

therefore, if the baseline system ($k_{\mathrm{GSL}} = 0$) satisfies Routh–Hurwitz, i.e., $\mathrm{tr}(A) < 0$ and $\det(A) > 0$, then any increase in $k_{\mathrm{GSL}} > 0$ strictly increases $\det(A)$ while leaving $\mathrm{tr}(A)$ unchanged. Hence, both eigenvalues shift leftwards and the small-signal damping of $V_{\mathrm{DC}}$ improves. Fig. 7 presents the root locus plots of the linearized system for four representative ZIP load scenarios: (i) P-dominated $(w_{\mathrm{P}}, w_{\mathrm{I}}, w_{\mathrm{Z}}) = (0.9, 0.1, 0.0)$, (ii) I-dominated $(0.1, 0.9, 0.0)$, (iii) Z-dominated $(0.1, 0.0, 0.9)$, and (iv) mixed $(0.3, 0.4, 0.3)$. The plots depict the trajectory of the system eigenvalues in the complex plane as the GSL gain $k_{\mathrm{GSL}}$ increases, providing insight into stability and damping behavior. In the Z-dominated case (Fig. 7a), the dominant poles initially shift leftward, enhancing damping, but move back toward the imaginary axis at higher gains, indicating reduced damping. The I-dominated case (Fig. 7b) shows a similar trend, with improved damping that saturates for large $k_{\mathrm{GSL}}$. In contrast, the P-dominated scenario (Fig. 7c) exhibits negligible eigenvalue movement, confirming limited influence of the GSL controller under constant-power loading. The mixed case (Fig. 7d) combines these effects, yielding moderate improvements. These results demonstrate that the stabilizing contribution of the GSL controller strongly depends on the ZIP composition: Z- and I-dominated loads benefit from moderate gains, whereas P-dominated loads remain largely unaffected, and excessive gains may even degrade damping. The GSL action induces a positive incremental input conductance $G_{\mathrm{gsl}}$ at the bus: a drop in $V_{\mathrm{DC}}$ lowers $V^*_{\mathrm{Ld}}$, which reduces $P_{\mathrm{out}}$ and thus $i'_{\mathrm{Ld}}$. This counters the negative-resistance tendency embedded in $a_{22}$ and increases $\det(A)$, thereby enhancing stability. The effect scales with the ZIP sensitivity $(P_I + 2P_Z)/V_0$, the gain $k_{\mathrm{GSL}}$, and the voltage ratio $\alpha = V^{\mathrm{nom}}_{\mathrm{Ld}}/V^*_{\mathrm{DC}}$.

As shown in this section, the incremental conductance induced by the GSL controller in (21) is proportional to $P_{\mathrm{I}} + 2P_{\mathrm{Z}}$. Consequently, for constant-current or impedance-dominated loads ($w_{\mathrm{I}} > 0$ and/or $w_{\mathrm{Z}} > 0$) the GSL action adds a strictly positive input conductance and improves small-signal damping. In contrast, for an ideal purely constant-power load ($w_{\mathrm{P}} = 1$) the sensitivity $\partial P_{\mathrm{Ld}}/\partial V_{\mathrm{Ld}}$ vanishes, $P_{\mathrm{I}} + 2P_{\mathrm{Z}} = 0$, and $G_{\mathrm{gsl}} = 0$, so the proposed GSL control has effectively no stabilizing effect in this case. The previous analysis assumes a fixed restoration state $\theta = 1$, representing the worst-case scenario of continuous grid-supportive action. In practice, however, the energy-based restoration mechanism introduces a slow variation in $\theta$. This effect is addressed in the following remark. The energy-based restoration loop (Sec. III-B) acts on a time scale of several seconds, i.e. two orders of magnitude slower than the electrical dynamics captured by $J$. Including $\theta(t)$ in the linearization therefore adds only a slowly varying gain factor and does not alter the qualitative conclusions drawn above.

## V. Simulation Results

Time-domain simulations are performed to evaluate the effectiveness of the proposed GSL control under load disturbances that exceed the rated power of the laboratory setup. The averaged state-space model described in Section II is used, with system parameters as listed in Table I. Due to the fact that the half-bridges are built using identical passive components, they are listed in the table with the representative values $R_\zeta, L_\zeta, C_\zeta$ with $\zeta \in \{\mathrm{B1}, \mathrm{PV}, \mathrm{Ld1}\}$. As the primary focus of the present work is not on the design of the primary controllers, the PI regulator parameters for current and voltage control are not listed here. The nominal DC-bus voltage is defined as $700\,\mathrm{V}$. A constant-impedance load step is connected at $5\,\mathrm{s}$ to the DC-bus and disconnected at $t = 7\,\mathrm{s}$ . The load step is chosen to induce a bus-voltage deviation exceeding $5\,\%$. The same load profile is used for all cases. Six scenarios are evaluated: constant-impedance load (CZL), constant-current load (CCL), and an equally shared ZIP case (each $1/3$), each tested with and without GSL control. Across all ZIP compositions, the GSL control reduces both the voltage sag during the load step and the overshoot during recovery. For the cases without GSL, the voltage responses remain similar, as the load power remains mostly unchanged due to the lack of voltage dependency in the control scheme. In contrast, the GSL-controlled responses vary significantly with load type due to their distinct voltage sensitivities. As seen in Fig. 8, the voltage-dependent behavior of the CZL case leads to a larger power drop than that of the CCL case, which aligns with the underlying ZIP model dynamics. The GSL control reduces the voltage dip in all scenarios. For the CZL case, the minimum voltage improves from $653.568\,\mathrm{V}$ to $678.47\,\mathrm{V}$, corresponding to a dip reduction from $46.43\,\mathrm{V}$ $(6.63\,\%)$ to $21.53\,\mathrm{V}$ $(3.08\,\%)$, i.e., a $53.6\,\%$ improvement. In the CCL case, the dip decreases from $45.99\,\mathrm{V}$ $(6.53\,\%)$ to $22.2\,\mathrm{V}$ $(3.17\,\%)$, resulting in a $51.58\,\%$ reduction. For the mixed ZIP case with equal weighting, the voltage recovers from a minimum of $653.74\,\mathrm{V}$ to $673.99\,\mathrm{V}$, reducing the dip from $46.257\,\mathrm{V}$ $(6.61\,\%)$ to $26.01\,\mathrm{V}$ $(3.71\,\%)$, which corresponds to a $43.8\,\%$ reduction. In the absence of GSL control, all evaluated load configurations result in voltage sags that exceed the standard $\pm 5\,\%$ tolerance band. The maximum deviations

TABLE I
Key Parameters of the Simulated DC Microgrid

| Symbol | Description | Value / Unit |
|---|---|---|
| | System Ratings – Simulation Model | |
| $V^*_{\mathrm{DC}}$ | Nominal DC-bus voltage | 700 V |
| $p_{\mathrm{PV,max}}$ | PV power rating | 90 kW |
| $p_{\mathrm{BESS,max}}$ | BESS power rating | 120 kW |
| $p_{\mathrm{Ld,max}}$ | Load power (aggregate) | 96 kW |
| | Converter Filter Components | |
| $R_\zeta$ | Converter line resistance (all) | $0.1\,\Omega$ |
| $L_\zeta$ | Converter filter inductance | 2.5 mH |
| $C_\zeta$ | Converter filter capacitance | 500 µF |
| $C_{\mathrm{DC}}$ | DC-bus capacitor | 2.2 mF |
| | Control and Sampling Parameters | |
| $f_{\mathrm{sw}}$ | Switching frequency | 20 kHz |
| $f_{\mathrm{s}}$ | Sampling frequency | 20 kHz |

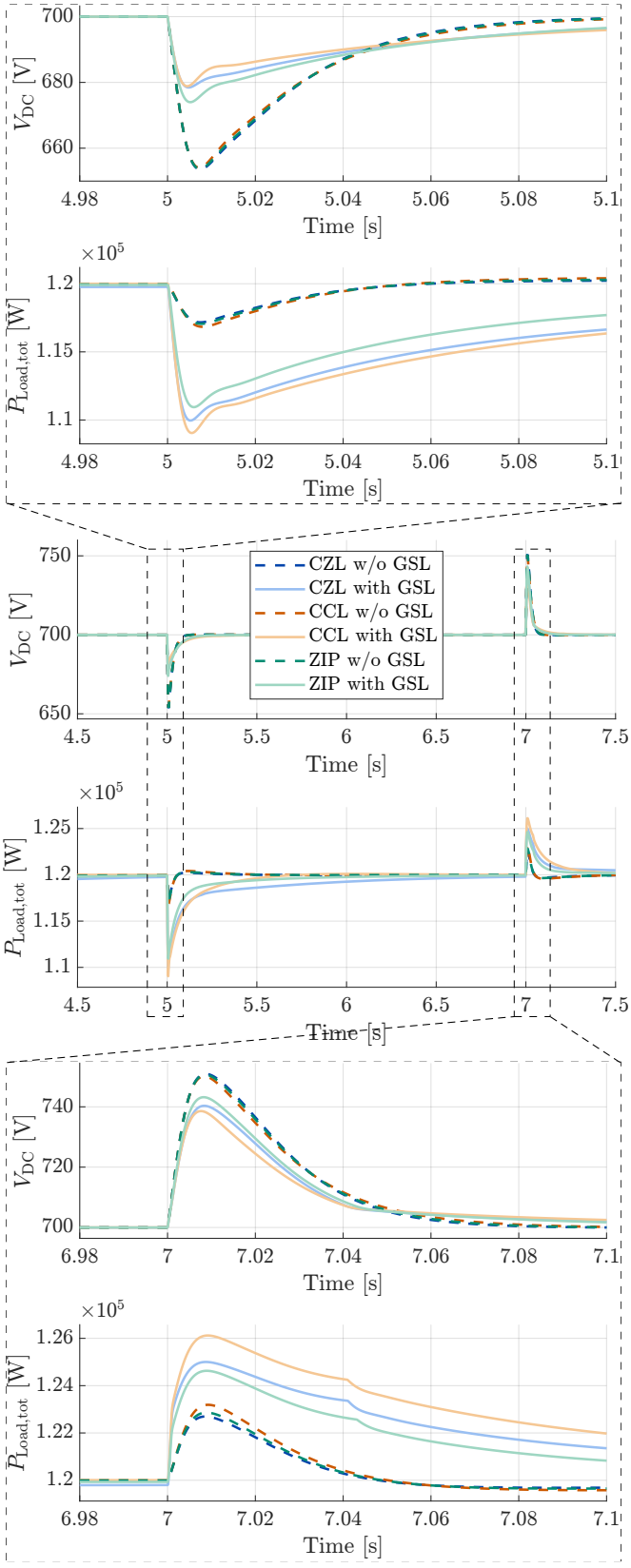


Fig. 8. DC-bus voltage $V_{\mathrm{DC}}$ and total load power $P_{\mathrm{load,tot}}$ for three load models with and without GSL: constant-impedance (CZL), constant-current (CCL), and mixed ZIP (one third each). A load step is applied at $t = 5\,\mathrm{s}$ and removed at $t = 7\,\mathrm{s}$.

from the nominal DC-bus voltage of $700\,\mathrm{V}$ reach $6.63\,\%$ for the constant-impedance load, $6.53\,\%$ for the constant-current load, and $6.61\,\%$ for the uniformly mixed ZIP load. With GSL control applied, the voltage dips are substantially mitigated and remain fully within the $\pm 5\,\%$ range for all scenarios. The respective deviations are reduced to $3.08\,\%$, $3.17\,\%$, and $3.71\,\%$, corresponding to relative reductions of $53.6\,\%$, $51.6\,\%$, and $43.8\,\%$, respectively. These results confirm that the proposed GSL approach effectively enhances voltage stability across a broad range of ZIP load compositions, without the need for communication or centralized coordination.

## VI. Experimental Validation

The proposed GSL method has been experimentally validated using a scaled down DC microgrid testbench, as depicted in Fig. 9 comprising a 3 kW photovoltaic (PV) emulator, a 10 kW BESS Emulator, and ZIP loads with dynamically adjustable constant impedance, current, and power components. The control and sampling parameters, as well as the converter filter components, are identical to those listed in Table I, while the hardware components of the experimental setup are summarized in Table II.

TABLE II
Hardware Components of the Experimental DC Microgrid

| Category | Component | Remarks |
|---|---|---|
| Control Platform | Imperix B-Box RCP | Dual-core ARM + Kintex FPGA, 250 kHz control |
| Power Converter | Imperix PEB8038 | SiC-MOSFET, 800 V, 38 A, 200 kHz |
| Current Sensor | Imperix DIN50 | 99 mV $\mathrm{A}^{-1}$, 200 kHz, isolated |
| Voltage Sensor | Imperix DIN800 | 2.46 mV $\mathrm{V}^{-1}$, >60 kHz, isolated |
| PV/Bat. Emulator | EA PSI 1000 / Delta SM15K-CP | Bidirectional, 15 kW, up to 1500 V |
| Progr. Loads | In-house design | Dynamic profiles, automated tests |
| Inductor | Hahn V23105 | 2.36 mH, 20 A |
| Capacitor | KEMET C274AC35100SA0J | 10 µF, damping / filtering |
| Resistor | Frizlen BW81 | 1 Ω-100 Ω, 10 kW, adjustable slide resistors |

The line resistances in Fig. 2 are all considered to be approximately $0.1\ \Omega$, while the capacitors are chosen $500\ \mu\mathrm{F}$ and the inductors are $2.5\ \mathrm{mH}$.

The performance of the proposed GSL method is evaluated by comparison with a standard Proportional-Integral (PI) control. In order to present a consistent comparison between the two control approaches, the influence of weather variations on the PV emulator system is excluded by maintaining a constant irradiance and temperature. To make the restoration mechanism observable within the short transient window, the maximum allowed energy deviation is deliberately set conservatively to $E_{\mathrm{GSL}}^{\max} = 1 \times 10^{-4}\,\mathrm{kW\,h}\ \left(= 0.1\,\mathrm{W\,h} \approx 360\,\mathrm{J}\right)$. This small budget forces the restoration loop to engage already during the dynamic transition, which represents a worst case for interaction with fast voltage support. In practical devices, the available flexibility is typically orders of magnitude larger

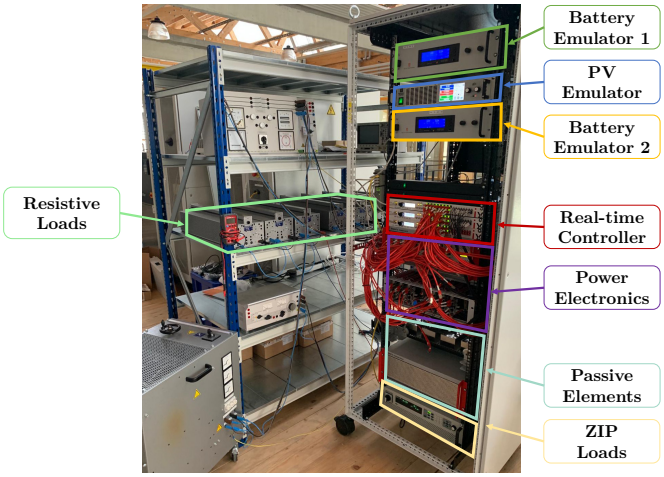


Fig. 9. DC microgrid setup consisting of a PV emulator, converter-based loads, real-time controller, passive components, and Battery emulators.

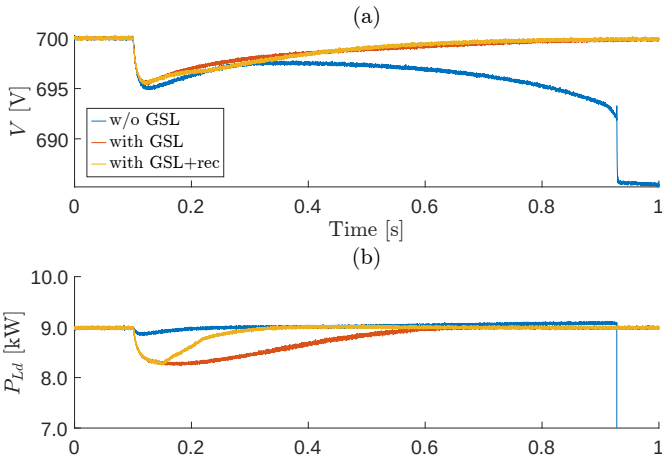


Fig. 11. Experimental results: without GSL (blue), with GSL (red), and with GSL and load restoration (yellow). (a) DC-bus voltage and (b) total load power.

(Wh to kWh range), so $E_{\mathrm{GSL}}^{\max}$ would be higher and restoration would act on a slower time scale with even less influence on the fast dynamics. The DC-bus operates at 700 V, with three

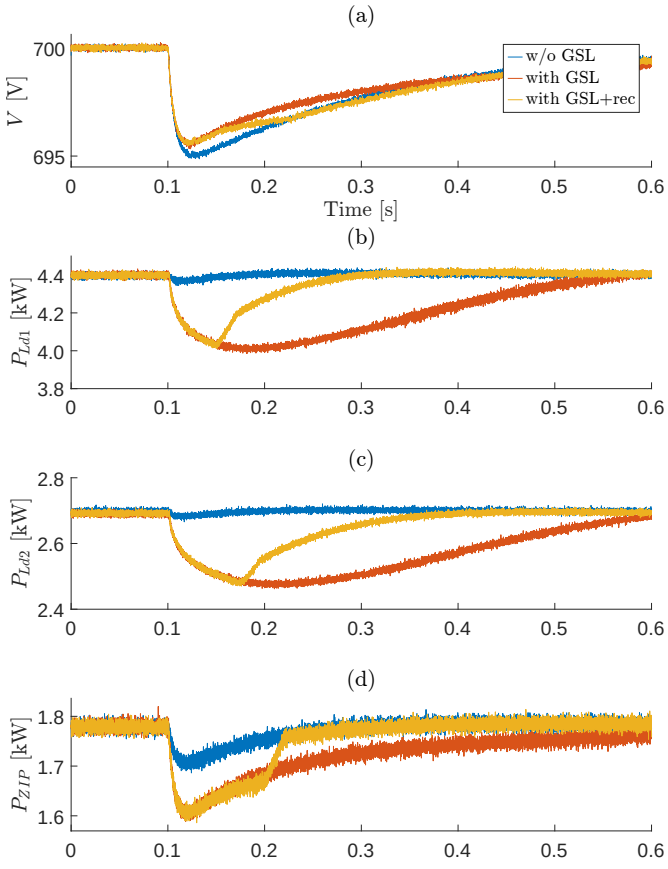


Fig. 10. Experimental results: without GSL (blue), with GSL (red), and with GSL and load restoration (yellow). (a) DC-bus voltage, (b) load 1 power, (c) load 2 power, and (d) ZIP load power.

load converters in the system. The first and second converters supply resistive loads of 4.4 kW and 1.8 kW, respectively. The third converter feeds a ZIP load with parameters $w_Z = 0.3$, $w_I = 0.2$, and $w_P = 0.5$, and a nominal power of 1.75 kW. At $t = 0.1$ s, a 4 kW load is directly connected to the DC-bus, resulting in a voltage drop. Fig. 10 illustrates the comparative performance of the control strategies: without GSL (blue), with GSL (orange), and with GSL and restoration (yellow). In Fig. 10(a), the voltage profiles show that the inclusion of GSL improves voltage dynamics, with further improvements observed when GSL with restoration is applied. Fig. 10(b), (c), and (d) depict the respective load powers for each case. In Fig. 11, the total load power is increased to 9 kW, and a 4 kW load step is introduced at $t = 0.1$ s. In this case, without GSL, the system fails due to the battery reaching its power limit. However, as demonstrated in Fig. 11, the inclusion of GSL enhances system reliability and prevents a system service discontinuity.

## VII. Conclusion

This paper has presented a communication-free grid-supportive-load (GSL) controller that equips converter-interfaced ZIP loads with fast, local voltage-support capability in low-voltage DC microgrids. The approach combines a saturation–hysteresis voltage map to guarantee device-level safety with an energy-based restoration scheme that bounds long-term energy deviation and ensures a smooth return to the nominal operating point. Analytical and simulation studies demonstrated that the proposed method enhances small-signal damping across different ZIP compositions. In particular, Z- and I-dominated scenarios benefited from improved stability margins, while the controller maintained bounded operation even under destabilizing constant-power loads. The results confirmed that the dynamic behavior observed in simulation closely aligns with the theoretical predictions. Experimental validation on a 700 V, 14 kW microgrid testbench further verified the effectiveness of the proposed concept. Under a 4 kW disturbance, the DC-bus voltage dip was reduced by 12.9 % compared to a cascaded-PI benchmark, and converter shutdown was successfully avoided. These outcomes underline the superiority of the proposed GSL control over conventional methods in practical settings. The presented findings highlight

the potential of GSLs as a scalable and low-cost means of providing ancillary services in converter-dominated DC networks. By relying solely on local voltage measurements, the method eliminates communication overhead and enables straightforward deployment at the demand side.

## REFERENCES


[1] A. Sauer, *The DC-Factory*, ser. Hanser eLibrary. München: Carl Hanser Verlag, 2021.

[2] P. Christensen et al., "High penetration of power electronic interfaced power sources and the potential contribution of grid forming converters," ENTSO-E, European Network of Transmission System Operators for electricity, Brussels, Belgium, Tech. Rep., 2020, eNTSO-E. [Online]. Available: https://strathprints.strath.ac.uk/72581/

[3] F. Perez and G. Damm, *Control and optimization of distributed energy storage systems*, ch. Chapter 5, pp. 93–119. [Online]. Available: https://digital-library.theiet.org/doi/abs/10.1049/PBPO214E_ch5

[4] T. A. Fagundes, G. H. F. Fuzato, L. J. R. Silva, A. M. d. S. Alonso, J. C. Vasquez, J. M. Guerrero, and R. Q. Machado, "Battery energy storage systems in microgrids: A review of soc balancing and perspectives," *IEEE Open Journal of the Industrial Electronics Society*, vol. 5, pp. 961–992, 2024.

[5] H. Jain, B. Mather, A. K. Jain, and S. F. Baldwin, "Grid-supportive loads—a new approach to increasing renewable energy in power systems," *IEEE Transactions on Smart Grid*, vol. 13, no. 4, pp. 2959–2972, 2022.

[6] Z. Mirza and H. Jain, "Implementing grid supportive behavior in induction motor-driven loads using field oriented control," in *2023 IEEE PES GTD International Conference and Exposition (GTD)*, 2023, pp. 28–32.

[7] F. Wald, Q. Tao, and G. De Carne, "Virtual synchronous machine control for asynchronous grid connections," *IEEE Transactions on Power Delivery*, vol. 39, no. 1, pp. 397–406, 2024.

[8] J. Geis-Schroer, Q. Tao, M. Courcelle, G. Bock, M. Suriyah, T. Leibfried, and G. D. Carne, "Power-to-frequency dependency of residential loads in a wider frequency range: An experimental investigation," *IEEE Transactions on Industry Applications*, vol. 60, no. 6, pp. 9184–9194, 2024.

[9] Y. Son, M. Blonsky, N. Guruwacharya, V. R. Chowdhury, and B. Mather, "Autonomous grid support functionality in variable-speed drive-based end-use loads," *IEEE Transactions on Power Electronics*, vol. 39, no. 10, pp. 12 177–12 182, 2024.

[10] Z. Mirza and H. Jain, "Automated fast frequency response from inverter-based motor loads," *IEEE Transactions on Smart Grid*, vol. 16, no. 4, pp. 2940–2952, 2025.

[11] H. Wang and F. Blaabjerg, "Reliability of capacitors for dc-link applications in power electronic converters—an overview," *IEEE Transactions on Industry Applications*, vol. 50, no. 5, pp. 3569–3578, 2014.

[12] Q. Peng, J. Fang, Y. Yang, T. Liu, and F. Blaabjerg, "Maximum virtual inertia from dc-link capacitors considering system stability at voltage control timescale," *IEEE Journal on Emerging and Selected Topics in Circuits and Systems*, vol. 11, no. 1, pp. 79–89, 2021.

[13] M. Ren, X. Sun, Y. Sun, K. Shi, and P. Xu, "A virtual inertial control strategy for bidirectional interface converters in hybrid microgrid," *International Journal of Electrical Power & Energy Systems*, vol. 153, p. 109388, 2023. [Online]. Available: https://www.sciencedirect.com/science/article/pii/S0142061523004453

[14] M. Anees, H. Tu, and S. Lukic, "Stability Considerations for Virtual Capacitor Control in Constant Power DC Loads," *IEEE Transactions on Power Electronics*, vol. 40, no. 4, pp. 4734–4739, 2025.

[15] X. Chen, M. Shi, H. Sun, Y. Li, and H. He, "Distributed cooperative control and stability analysis of multiple dc electric springs in a dc microgrid," *IEEE Transactions on Industrial Electronics*, vol. 65, no. 7, pp. 5611–5622, 2018.

[16] H. Yang, T. Li, Y. Long, C. L. P. Chen, and Y. Xiao, "Distributed virtual inertia implementation of multiple electric springs based on model predictive control in dc microgrids," *IEEE Transactions on Industrial Electronics*, vol. 69, no. 12, pp. 13 439–13 450, 2022.

[17] M. Anees, H. Tu, and S. Lukic, "Design Considerations for Load Droop Control in DC Systems," *IEEE Transactions on Power Electronics*, vol. 41, no. 2, pp. 1539–1545, 2026.

[18] Ö. Ekin, A. Balakrishnan, L. Spatafora, and V. Hagenmeyer, "Distributed control strategy for grid supportive loads in dc microgrids," in *2024 9th IEEE Workshop on the Electronic Grid (eGRID)*, 2024, pp. 1–6.

[19] Ö. Ekin, J. Galenzowski, G. De Carne, and V. Hagenmeyer, "Grid-supportive load control in dc microgrids using hysteresis-based voltage regulation," in *2025 IEEE Kiel PowerTech*, 2025, pp. 1–6.

[20] S. Bahrami, S. S. Mousavi, and M. Shafiee-Rad, "Decentralized adaptive nonlinear controller for voltage regulation of output-constrained dc microgrids with zip loads," *IEEE Transactions on Power Systems*, vol. 39, no. 5, pp. 6210–6221, 2024.

[21] S. M. H. Rizvi, S. K. Sadanandan, and A. K. Srivastava, "Real-time parameter tracking of power-electronics interfaced composite zip load model," *IEEE Transactions on Smart Grid*, vol. 13, no. 5, pp. 3891–3902, 2022.


**Ömer Ekin** (Graduate Student Member, IEEE) received the M.Sc. degree in electrical engineering and information technology from the Karlsruhe Institute of Technology, Karlsruhe, Germany, in 2021. He is currently working toward the Ph.D. degree at the Institute for Automation and Applied Informatics at the Karlsruhe Institute of Technology, where his research includes modeling and control of power systems and microgrids.

**Moein Ghadrdan** (Member, IEEE) received the B.Sc. degree in Electrical Engineering from Iran University of Science and Technology, Tehran, Iran, in 2015, and the M.Sc. and Ph.D. degrees in Electrical Engineering from Sharif University of Technology, Tehran, Iran, in 2017 and 2022, respectively. From 2021 to 2022, he was a Visiting Ph.D. Scholar with the AAU Energy Department, Aalborg University, Aalborg, Denmark. Since 2024, he has been a Postdoctoral Researcher with the Institute for Technical Physics, Karlsruhe Institute of Technology, Karlsruhe, Germany. His research interests include DC grids protection and reliability-oriented design of power systems.

**Giovanni De Carne** (Senior Member, IEEE) received the B.Sc. and M.Sc. degrees in electrical engineering from the Polytechnic University of Bari, Italy, in 2011 and 2013, respectively, and the Ph.D. degree from the Chair of Power Electronics, Kiel University, Germany, in 2018. Prof. De Carne is currently W3 (full) professor at the Institute for Technical Physics at the Karlsruhe Institute of Technology, Karlsruhe, Germany, where he leads the "Real Time Systems for Energy Technologies" Group and the "Power Hardware In the Loop Lab". He is currently supervising PhD students, managing academic and industrial projects, and developing multi-MW power hardware in the loop testing infrastructures for energy storage systems and hydrogen-based technologies. He has authored/co-authored more than 100 peer-reviewed scientific papers. His research interests include power electronics integration in power systems, solid-state transformers, real-time modelling, and power hardware in the loop. Prof. De Carne is currently in the PELS AdCom Member-at-Large and Co-EiC of the IEEE Open Journal of Power Electronics.

**Veit Hagenmeyer** (Member, IEEE) is Professor of Energy Informatics at the Department of Informatics and Director of the Institute for Automation and Applied Informatics at Karlsruhe Institute of Technology (KIT), Germany. His research interests include the modeling, optimization, and control of sector-integrated energy systems; machine-learning-based forecasting of uncertain demand and generation in energy systems predominantly driven by renewable energies; and the integrated cybersecurity of such systems. Before his professorship, he served as power plant director responsible for three power plants and the energy network of BASF at the Ludwigshafen site in Germany. He is the spokesperson for the national "Energy System Design" program of the Helmholtz Association and the founding director of the national BMBF Kopernikus ENSURE project for new grid structures. He also serves as the actual spokesperson of the Energy Lab at KIT and the associated Living Lab Energy Campus project. He is President of the European Institute for Energy Research and a member of the Scientific Advisory Board of Électricité de France.